

The GREGOR Fabry-Pérot Interferometer

K.G. Puschmann^{1,*}, C. Denker¹, F. Kneer², N. Al Erdogan³, H. Balthasar¹, S.M. Bauer¹, C. Beck⁴, N. Bello González⁵, M. Collados⁴, T. Hahn¹, J. Hinzberger⁶, A. Hofmann¹, R.E. Louis¹, H. Nicklas², O. Okunev⁷, V. Martínez Pillet⁴, E. Popow¹, T. Seelemann⁸, R. Volkmer⁵, A.D. Wittmann², and M. Woche¹

¹ Leibniz-Institut für Astrophysik, An der Sternwarte 16, 14482 Potsdam, Germany

² Institut für Astrophysik, Georg-August-Universität Göttingen, Friedrich-Hund-Platz 1, 37077 Göttingen, Germany

³ Department of Astronomy and Space Sciences, University Istanbul, 34134 Vezneciler/Istanbul, Turkey

⁴ Instituto de Astrofísica de Canarias, C/ Vía Láctea s/n, 38205 La Laguna, Tenerife, Spain

⁵ Kiepenheuer-Institut für Sonnenphysik, Schöneckstraße 6, 79104 Freiburg, Germany

⁶ Max-Planck-Institut für Sonnensystemforschung, Max-Planck-Straße 2, 37191 Katlenburg-Lindau, Germany

⁷ Central Astronomical Observatory, Russian Academy of Sciences, Pulkovskoye Chaussee 65/1, 196140 St. Petersburg, Russia

⁸ LaVision, Anna-Vandenhoeck-Ring 19, 37081 Göttingen, Germany

Received November 27, 2024, accepted later

Published online later

Key words Sun: photosphere — Sun: magnetic fields — instrumentation: interferometers — instrumentation: polarimeters — techniques: spectroscopic — techniques: high angular resolution

The GREGOR Fabry-Pérot Interferometer (GFPI) is one of three first-light instruments of the German 1.5-meter GREGOR solar telescope at the Observatorio del Teide, Tenerife, Spain. The GFPI uses two tunable etalons in collimated mounting. Thanks to its large-format, high-cadence CCD detectors with sophisticated computer hard- and software it is capable of scanning spectral lines with a cadence that is sufficient to capture the dynamic evolution of the solar atmosphere. The field-of-view (FOV) of $50'' \times 38''$ is well suited for quiet Sun and sunspot observations. However, in the vector spectropolarimetric mode the FOV reduces to $25'' \times 38''$. The spectral coverage in the spectroscopic mode extends from 530–860 nm with a theoretical spectral resolution of $\mathcal{R} \approx 250,000$, whereas in the vector spectropolarimetric mode the wavelength range is at present limited to 580–660 nm. The combination of fast narrow-band imaging and post-factum image restoration has the potential for discovery science concerning the dynamic Sun and its magnetic field at spatial scales down to ~ 50 km on the solar surface.

© 2012 WILEY-VCH Verlag GmbH & Co. KGaA, Weinheim

1 Introduction

The recently inaugurated 1.5-meter GREGOR solar telescope (Schmidt et al. 2012a; Volkmer et al. 2010) is a new solar facility with the potential for cutting-edge science at fundamental scales, i.e., the pressure scale-height, the photon mean-free path, and the intrinsic size of elemental magnetic structures. The key science topics of the GREGOR telescope are (see Schmidt et al. 2012b): (1) the interaction between convection and magnetic fields in the photosphere, (2) the nature and dynamics of sunspots and pores and their temporal evolution, (3) the solar magnetism and its role in solar variability, and (4) the enigmatic heating mechanism of the chromosphere. The GREGOR telescope is equipped with powerful post-focus instrumentation for different wavelength regimes and science targets. The GRating Infrared Spectrograph (GRIS, Collados et al. 2008, 2012) and the GREGOR Fabry-Pérot Interferometer (GFPI) focus on spectropolarimetry in the near infrared and visible

spectral ranges, respectively. Both instruments are accompanied by the Broad-Band Imager (BBI, von der Lühse et al. 2012) for high-cadence, high-resolution imaging.

The roots of the GFPI can be traced back to 1986, when the Universitäts-Sternwarte Göttingen started to develop an imaging spectrometer for the German Vacuum Tower Telescope (VTT). This instrument used a universal birefringent filter (UBF) as an order-sorting filter for a narrow-band FPI mounted in a collimated light beam (Bendlin et al. 1992). The UBF was later replaced by a second etalon (Volkmer et al. 1995) and the spectrometer was equipped with a Stokes-V polarimeter (Koschinsky et al. 2001).

First ideas concerning an imaging spectrometer at the GREGOR telescope have been published by Kneer & Hinzberger (2001) and Kneer et al. (2003). A renewal of the Göttingen FPI during the first half of 2005 was, however, the first fundamental step towards the development of the GFPI (Puschmann et al. 2006). This included the integration of narrow-band etalons with diameters of 70 mm and large-format, high-cadence CCD detectors, both accompanied by sophisticated computer hard- and software.

* Corresponding author: e-mail: kgp@aip.de

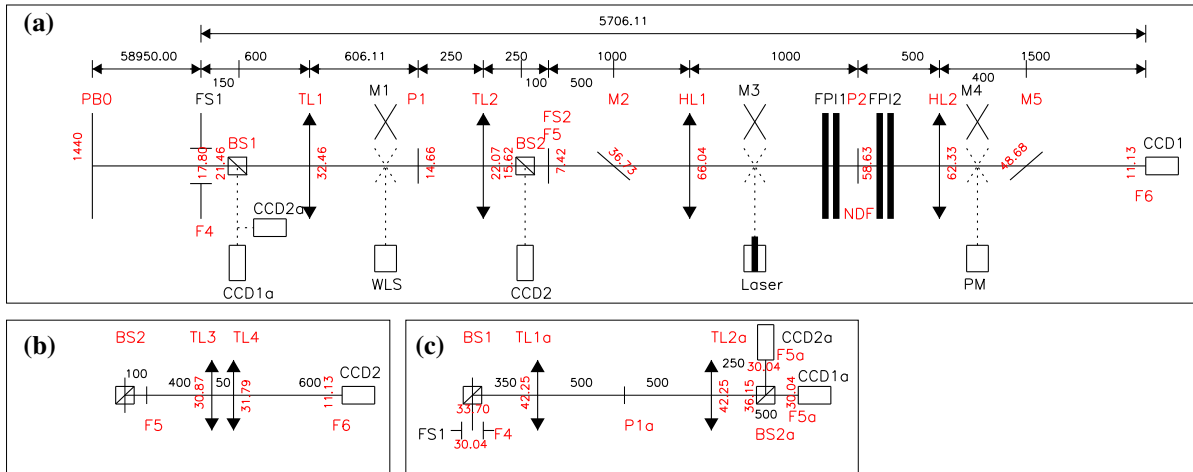


Fig. 1 Schematic design of the main channels of the GFPI: narrow-band channel NBC (a), broad-band channel BBC (b), and blue imaging channel BIC (c). The optical elements of the BIC are labeled with an extra ‘a’ (see text and Tab. 1 for details). The auxiliary channels, i.e., a laser-photomultiplier channel (Laser, PM) and a white-light channel (WLS) are only depicted in an illustrative way. All the distances are shown in millimeters.

40 From 2006 to 2007, the optical design of the GFPI was finalized and all relevant optical and opto-mechanical components were bought or manufactured (Puschmann et al. 2007). Subsequently, an upgrade to full-Stokes spectropolarimetry followed (Balthasar et al. 2009; Bello González & Kneer 2008).

45 In 2009, the Leibniz-Institut für Astrophysik Potsdam took over the scientific responsibility for the GFPI, and the instrument was finally installed at the GREGOR solar telescope (Denker et al. 2010). The integration of three computer-controlled translation stages (two filter sliders and one mirror stage) and the preparation of the software for TCP/IP communication with external devices according to the Device Communication Protocol (DCP, Halbgewachs et al. 2012) followed during the commissioning phase in 2011 (Puschmann et al. 2012a).

50 The current state of the instrument, including advanced and automated calibration and observing procedures and a new blue imaging channel (380–530 nm), is described in Puschmann et al. (2012b). Beside an inspection of first observational results obtained with the GFPI at the GREGOR telescope, the latter publication also includes a design concerning optics, cameras, and etalons for the future integration of the BLue Imaging Solar Spectrometer (BLISS), a second Fabry-Pérot for the wavelength range 380–530 nm that has been suggested by Denker (2010). Thus, Puschmann et al. (2012a,b) and the detailed description presented here give a complete overview of the present state of the instrument at the end of the 2012 science verification campaigns and its foreseen use at the GREGOR solar telescope.

70 Starting in 2002, many colleagues have contributed to the GFPI, which has been developed at the Institut für

Table 1 Properties of the main optical components of the GFPI.

Optical element	Focal length [mm]	Diameter [mm]	Optical element	Dimension [mm × mm]
TL1	600	63	BS1	40 × 40
TL2	250	40	BS2	40 × 40
HL1	1000	80	BS2a	40 × 40
HL2	1500	100	M2	60 × 85
TL3	400	63	M5	60 × 85
TL4	600	63		
TL1a	500	63		
TL2a	500	80		

Astrophysik Göttingen and at the Leibniz-Institut für Astrophysik Potsdam. In the spirit of this special issue of *Astronomische Nachrichten/AN*, the extensive list of co-authors honors all contributions to this instrument over the years. Details about the individual contributions can be glimpsed from the articles in the above chronology.

2 Optical design

80 The GFPI is fed with light from the telescope by a dichroic pentaprism that is located behind the adaptive optics just before the science focus F4. The pentaprism transmits the infrared wavelength range towards GRIS and reflects the visible wavelength range towards GFPI. The currently available pentaprism splits the light at 660 nm and thus permits GFPI observations at wavelengths shorter than H α . In the near future, a second pentaprism will enable observations of H α and the Ca II infrared lines around 850 nm, although the suitability of the GFPI cameras for the latter has still to be investigated because of the detector’s low quantum efficiency (< 15%) at infrared wavelengths (see Sect. 3).

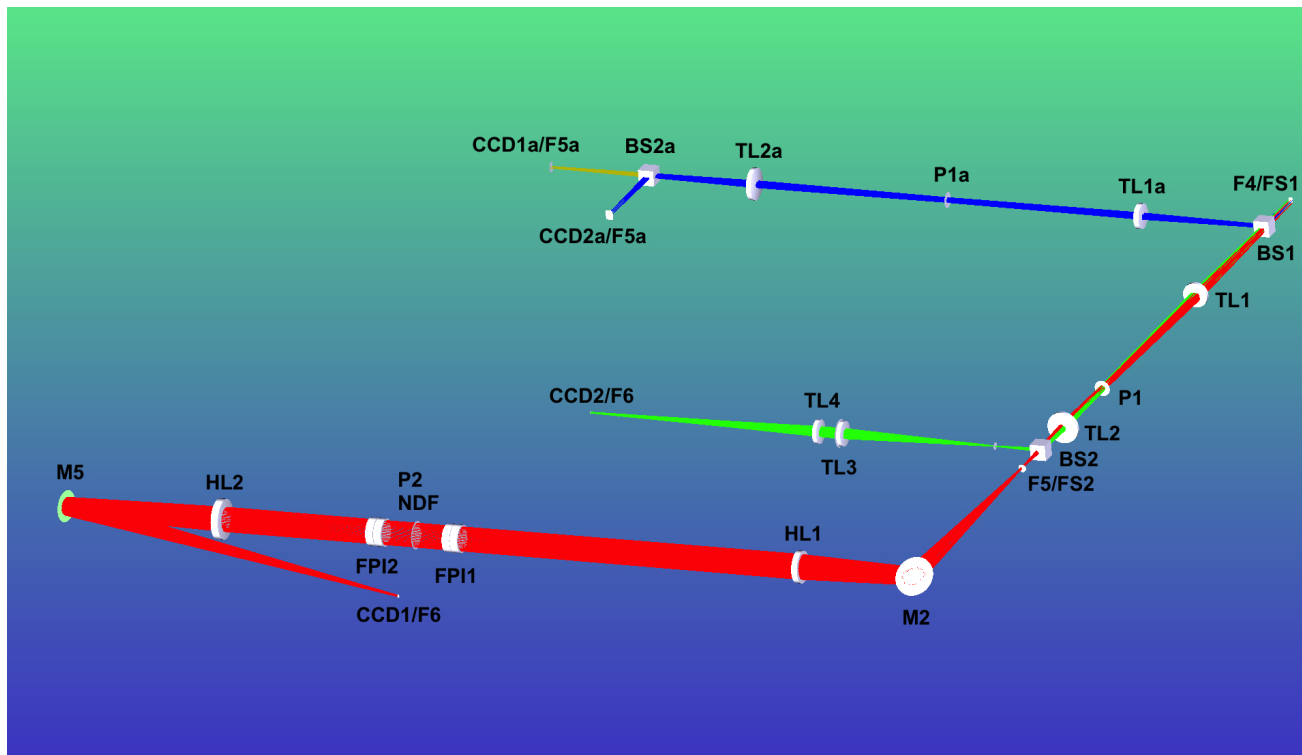


Fig. 2 NBC (red), BBC (green), and BIC (blue) in a ZEMAX multi-configuration file in shaded modeling for the respective central wavelength and maximal field dimension of each beam. The optical elements of the BIC are labeled with an extra 'a' (see text and Tab. 1 for details).

Figure 1 shows a schematic design of the current setup of the main components of the GFPI, i.e., the narrow-band channel (NBC, panel a), the broad-band channel (BBC, panel b), and the blue imaging channel (BIC, panel c). This design is based on calculations following geometrical optics, a strategy that was also the base for the original design of the GFPI presented in Puschmann et al. (2007, their Fig. 1). The diameter of the light beam at the different foci, pupils, and on the relevant optical surfaces is indicated together with an illustration of the auxiliary beams of the instrument. The focal lengths and diameters of individual lenses and the dimensions of other optical elements are summarized in Tab. 1. As in 2007, the calculations based on geometrical optics were confirmed by a ZEMAX ray-tracing as shown in Fig. 2.

The entire optical setup of the GFPI, including details about the auxiliary channels, i.e., the laser-photomultiplier channel and the white-light channel for etalon adjustment and spectral calibration purposes, as well as the distribution of all optical elements on the optical tables, can be found in a drawing up to scale in Puschmann et al. (2012b, their Fig. 1).

In the NBC of the GFPI, the science focus F4 is re-imaged twice by the achromatic lenses TL1, TL2, HL1, and HL2. This creates two foci (F5 and F6) and two pupil images (P1 and P2). The re-imaging is used to achieve a proper size of the pupil image P2 that is limited by the free aperture of the two etalons (FPI1 and FPI2), which are mounted close

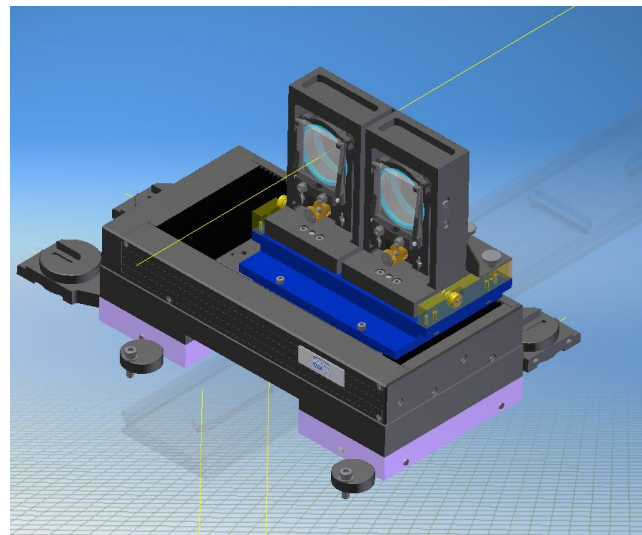


Fig. 3 CAD of the filter sliders mounted in NBC and BBC.

to the pupil image in a collimated light beam. A neutral density filter (NDF) of high optical quality between FPI1 and FPI2 reduces the inter-etalon reflexes. The beam in NBC is folded twice by the two deflection mirrors M2 and M5. Two field stops FS1 and FS2 prevent an over-illumination of the detectors. Furthermore, FS2 can be adjusted to avoid an overlap of the two images

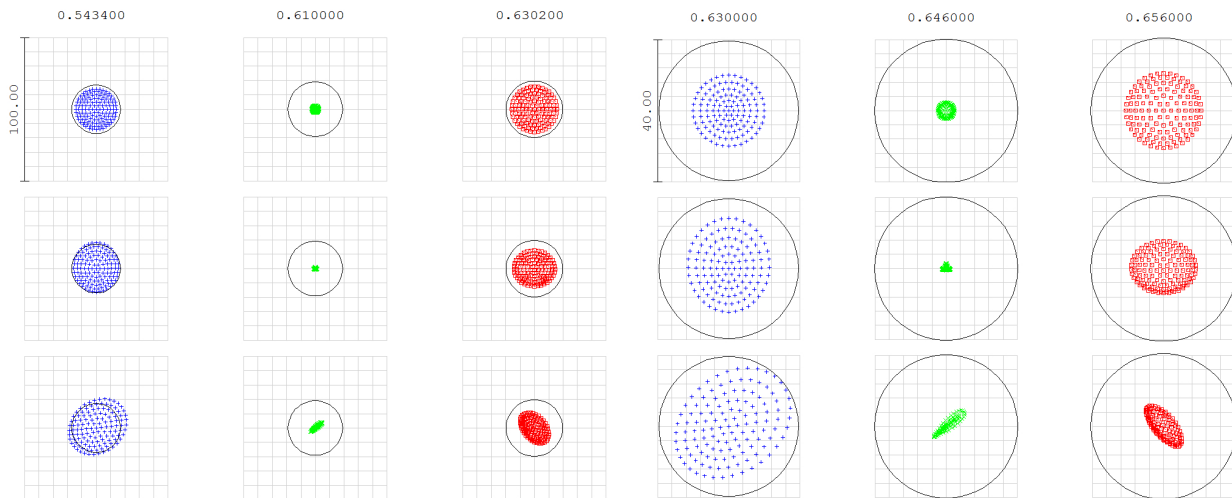


Fig. 4 Matrix spot diagrams of the NBC for different wavelengths and fields. In each panel the top row represents the optical axis, whereas the the middle and bottom row represents a field point at the middle right and in the diagonal corner on the detector, respectively. Left panel: wavelength range 543.4–630.2 nm with 610 nm in focus. Right panel: wavelength range 630–656 nm with 646 nm in focus. All spots inside the Airy-disk (circles in the boxes) are diffraction limited. The box sizes of 100 μm and 40 μm correspond to $0''.56$ and $0''.22$, respectively.

created by the removable dual-beam full-Stokes polarimeter. A beam splitting cube BS2 in front of F5 deflects 5% of the light into the BBC, where F5 is re-imaged by the achromatic lenses TL3 and TL4.

In the NBC and BBC, two computer-controlled filter sliders (see Fig. 3) allow one to sequentially observe two different wavelength bands. The filters restrict the band-pass for BBC and NBC to a full-width-at-half-maximum (FWHM) of 10 nm and 0.3–0.8 nm, respectively. Narrow-band filters with a FWHM in this range provide a good compromise between parasitic light, transmission, and signal-to-noise. The pre-filters of each channel can be tilted to optimize the wavelength of the transmission maximum. The sliders are limited to two interference filters because of the free space available in the NBC. The near-focus position of the filter sliders additionally required a high precision in the positioning of the pre-filters down to a few micrometers, which would have not been achievable with standard filter wheels. First science verification campaigns at GREGOR revealed the need for very long exposure times (up to 100 ms) in the NBC at full resolution of the cameras, when using filters with a transmission $T \approx 40\%$, e.g., for spectral scans of the Fe I $\lambda 543.4$ nm and Fe I $\lambda 557.6$ nm lines. A 2×2 -pixel binning of the CCDs reduces significantly the exposure times and increases the frame rate from 7 to 16 frames s^{-1} . Filters with $T \approx 80\%$, e.g., for spectral scans of the Fe I $\lambda 617.3$ nm and Fe I $\lambda 630.2$ nm lines, yield reasonable frame rates and exposure times even without binning (see Puschmann et al. 2012b).

In both NBC and BBC, Sensicam QE CCD detectors (CCD1 and CCD2) with an identical image scale at F6 are used for simultaneous data acquisition. Co-temporal recorded broad- and narrow-band data are fundamental for

a post-facto image restoration, which improves the spatial resolution of the data far beyond the real-time correction provided by the GREGOR Adaptive Optics System (GAOS, Berkefeld et al. 2012). A data pipeline is nearly finished (see Puschmann et al. 2012b), which includes both speckle and blind deconvolution reconstruction methods. A comparison of different methods, their application, and their results is given by Puschmann & Beck (2011).

A pentaprism BS1 deflects all wavelengths below 530 nm into the BIC, where F4 is re-imaged by two achromatic lenses (TL1a and TL2a). A 50/50 beam splitting cube finally directs the light onto two pco.4000 cameras that are in stock at the observatory. Different available pre-filters, e.g., at Ca II H $\lambda 396.8$ nm, the Fraunhofer G-band $\lambda 430.7$ nm, and a blue continuum window $\lambda 450.6$ nm with a FWHM = 1 nm and $T = 60\%$, can be placed in front of these two cameras for complementary high-cadence imaging.

All achromats used in the GFPI have been purchased off-the-shelf. Thus, the instrument is not super-achromatic. Observations in two different wavelength bands are restricted to a maximum wavelength separation of about 100 nm. Figure 4 shows matrix spot diagrams of the NBC for the case of multi-wavelength observations in the wavelength bands 543.4–630.2 nm (left panel) and 630–656 nm (right panel) with the cameras focused at 610 and 646 nm, respectively. Both panels exhibit the typical behavior of achromatic lens systems, when observing at wavelengths either to the red or blue of the wavelength in focus. At the edge wavelengths, the dots show a larger spread on-axis (top row of Fig. 4), which is accompanied by a directional component off-axis (bottom row of Fig. 4). For a large wavelength separation from the central wavelength in focus, the

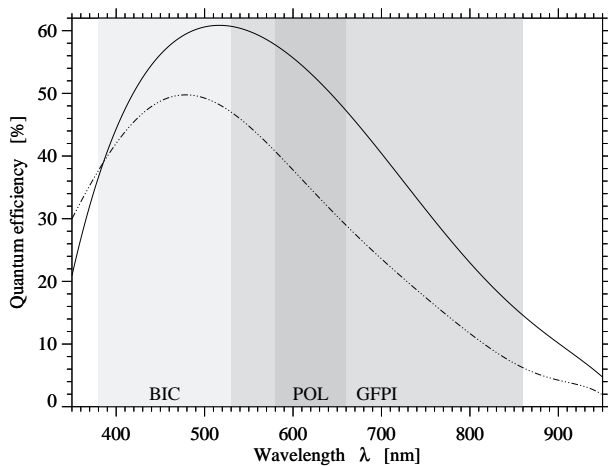


Fig. 5 Quantum efficiency of the Sensicam QE CCD (solid) and pco.4000 (dash-dotted) cameras. The different grey levels denote the respective wavelength ranges for the GFPI in spectroscopic (grey) and vector-polarimetric mode (dark grey), and for the blue imaging channel BIC (light grey).

spread of the dots exceeds the Airy disk and the performance is no longer diffraction-limited (e.g., lower leftmost panel). Modern achromatic lenses such as those of Quioptiq used in the GFPI are matched for the $H\alpha$ $\lambda 656.3$ nm and $H\beta$ $\lambda 486.1$ nm lines with a remaining variation of the focus position at 546 nm typically below 0.1%. As a consequence, we find a chromatic focus shift when observing away from the wavelength in focus. The different imaging quality between the left and the right panel is caused by the smaller spectral range used in the right panel and the stronger non-linearity of the chromatic focal shift in the spectral range for the left panel.

3 Cameras and control software

NBC and BBC are equipped with Sensicam QE CCD cameras with an analog-digital conversion with 12-bit resolution. Their Sony ICX285AL detectors have a full-well capacity of 18,000 e^- and a read-out noise of 4.5 e^- . Their quantum efficiency (QE) is depicted in Fig. 5 with a maximum of $\approx 60\%$ at 550 nm. The detectors have 1376×1040 pixels with a size of $6.45 \mu\text{m} \times 6.45 \mu\text{m}$. The spatial sampling per pixel is $0''.0361$ (see Puschmann et al. 2012b, their Tab. 3). Consequently, a field-of-view (FOV) of $50'' \times 38''$ is available in the spectroscopic mode of the instrument.

The cameras have a maximum frame rate at full resolution of 10 Hz. As mentioned before, long exposure times can further reduce the read-out frequency. This is especially problematic when using the instrument in full-Stokes mode. There, the duration of spectral line scans can increase to a few minutes when repeated images in the four different polarimetric states at up to 80 different wavelength positions are taken to improve the signal-to-noise ratio. Therefore, it

Table 2 Properties of the GFPI image acquisition system.

	NBC and BBC	BIC
Camera	2 × Imager QE	2 × pco.4000
Detector type	CCD	CCD
Pixels	1376×1040	2000×2672
Pixel size [μm^2]	6.45×6.45	9.0×9.0
Read out noise [e^-]	4.5	11
Full well capacity [e^-]	18,000	60,000
Spectral resp. [nm]	320–900	320–900
Quantum efficiency	60% @ 550 nm 45% @ 530 nm	32% @ 380 nm 54% @ 530 nm
Digitization [bit]	12	14
FOV	$50'' \times 38''$	$63'' \times 84''$
Image scale	$0''.0361 \text{ pixel}^{-1}$	$0''.0315 \text{ pixel}^{-1}$
Frame rate [Hz]	10	2.3

is presently recommended to use these cameras with a 2×2 -binning for such data, which still yields a spatial resolution of up to $0''.14$. By this, the intensity increases by a factor of four, resulting in shorter exposure times and much higher frame rates of up to 20 Hz. Polarimetry with the GFPI would certainly benefit by a future replacement of these cameras by modern sCMOS cameras with frame rates of up to 40 Hz without any binning (see Puschmann et al. 2012b).

For imaging in the BIC, two pco.4000 cameras are available at the observatory. Their detectors have a full-well capacity of 60,000 e^- and a read-out noise of 11 e^- . The frame rate of these cameras is limited to 2.3 Hz at full chip size using only one analog-digital converter. The QE is shown in Fig. 5, with $\approx 32\%$ ($\approx 54\%$) at a wavelength of 380 (530) nm. With a pixel size of $9 \mu\text{m} \times 9 \mu\text{m}$, their 4008×2672 pixels yield a total chip size of $36 \text{ mm} \times 24 \text{ mm}$. The image scale at both cameras is $0''.0315 \text{ pixel}^{-1}$. A field stop in F4 avoids a vignetting of the blue beam. The illuminated part of the sensor thus corresponds to only 2000×2672 pixels, yielding a FOV of $63'' \times 84''$. With the reduced read-out area on the chip, the cameras permit the recording of more than 30 images in less than 15 s, which is sufficient to allow for post-facto image reconstruction. However, BIC is just an intermediate solution and will be replaced by the Blue Imaging Solar Spectrometer (BLISS, Puschmann et al. 2012b) in the near future. A summary of the properties of the GFPI image acquisition systems can be found in Tab. 2.

The communication between internal (cameras, etalons, polarimeter, and filter and mirror sliders) and peripheral devices (telescope, AO system, AO filter wheel, GPU, GRIS, etc.) is controlled by the software package DaVis from LaVision in Göttingen. Its first adaptation to the spectrometer, including a description of the resulting Graphical User Interface (GUI) and required scan tables, is described in detail in Puschmann et al. (2006). The modification of the software for TCP/IP communication with external devices using DCP and the subsequent implementation of automated observing and calibration procedures is depicted in (Puschmann et al. 2012a,b). Puschmann et al. (2012a, their

Table 3 Etalon- and spectral properties of the GFPI.

	Etalon 1	Etalon 2
Manufacturer	ICOS	ICOS
Diameter [mm]	70	70
Finesse	46	46
Reflectivity [%]	95	95
Etalon spacing [mm]	1.1	1.4
FWHM [pm] @ 617 nm	3.43	2.73
FWHM combined [pm] @ 617 nm	1.95	
Spectral resolution	250,000	
Parasitic-light fraction [%]	≈ 1.0	
Controllers	CS-100 (ICOS)	
Spectral scanning	RS-232	
Coating	530–860 nm	

Note: The parasitic-light fraction is given for a pre-filter with FWHM = 0.3 nm and is valid for the entire wavelength range.

Fig. 2) shows a flow chart of the communications of the GFPI control computer (DaVis) with all internal and peripheral devices.

4 Dual etalon system

The central optical element of the GFPI is a dual-etalon system, which is mounted in the collimated beam close to a pupil image with a 58 mm diameter. The etalon properties and theoretical spectral characteristics of the instrument are summarized in Tab. 3 and are described in detail below.

The normalized transmission profile of a single etalon is given by

$$\frac{I}{I_0} = \frac{T}{1 + F \sin^2 \delta/2} \quad (1)$$

$$T = \left(1 - \frac{A}{1 - R}\right)^2 \quad (2)$$

$$F = \frac{4R}{(1 - R)^2} \quad (3)$$

$$\delta = \frac{4\pi n d \cos \theta}{\lambda} + 2\Phi \quad (4)$$

with the incident intensity I_0 , transmitted intensity I/I_0 , reflectivity R , absorption A , peak transmission T , phase difference δ , index of refraction n , plate spacing of the etalons d , angle of incidence θ , phase change on internal reflections Φ , and wavelength λ .

The plate spacings of the two narrow-band etalons are $d_1 = 1.100$ mm and $d_2 = 1.408$ mm because of historical reasons (see below) and were provided by IC Optical Systems (ICOS) with an accuracy of ± 1 μ m. Somewhat larger deviations from the nominal values were observed, while determining the precise step ratios, which are required to tune the etalons in tandem. However, these small deviations are of no consequence for the following discussion of the etalon characteristics. The manufacturer also furnished

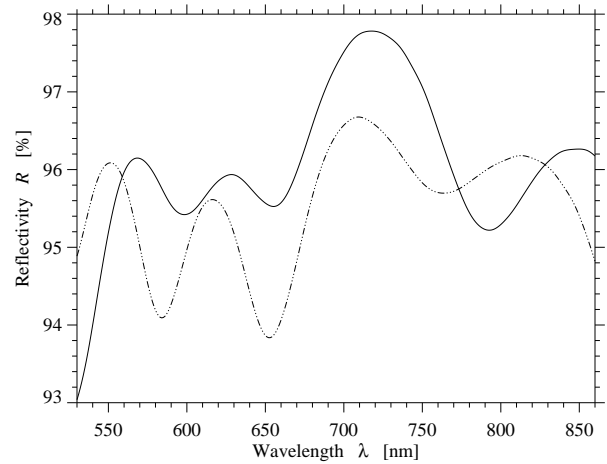


Fig. 6 Reflectivity R_1 of the broad-band (dash-dotted) and R_2 of the narrow-band (solid) etalon coating curves.

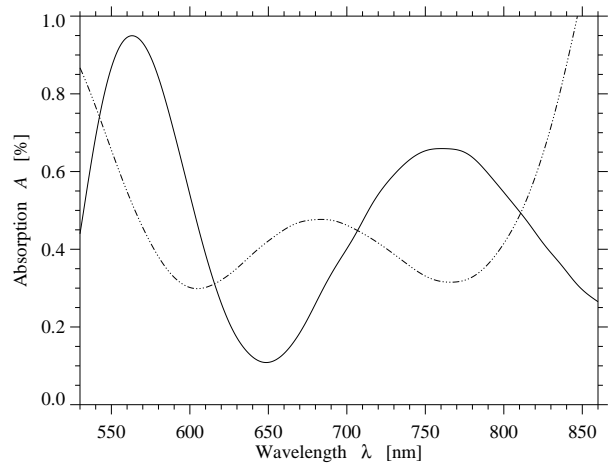


Fig. 7 Absorption A_1 of the broad-band (dash-dotted) and A_2 of the narrow-band (solid) etalon coating curves.

the coating curves for both etalons. The reflectivity $R_{1,2}$ and absorption $A_{1,2}$ curves are shown in Figs. 6 and 7, respectively. A nominal reflectivity $R = 96\%$ and absorption $A = 0.5\%$ was specified as the goal for the wavelength range 530–860 nm. In practice, flat coating curves covering such a broad wavelength range cannot be achieved. In general, the deviations from the nominal values are small. Only toward the blue and infrared stronger departures from the nominal values are observed, so that observations outside the bounds of the wavelength region are not impossible but the performance of the etalons will decrease significantly.

The peak transmissions $T_{1,2}$ depend only on the reflectivities $R_{1,2}$ and absorptions $A_{1,2}$ of the two etalons (Eq. 2). The combined peak transmission T is simply the product of T_1 and T_2 . The corresponding transmission curves in Fig. 8 demonstrate clearly that FPIs can achieve nowadays a very high transmission, i.e., 60–90% in case of a single etalon and 40–80% for a dual-etalon system. The peak transmission of the GFPI exceeds 60% in the wavelength range

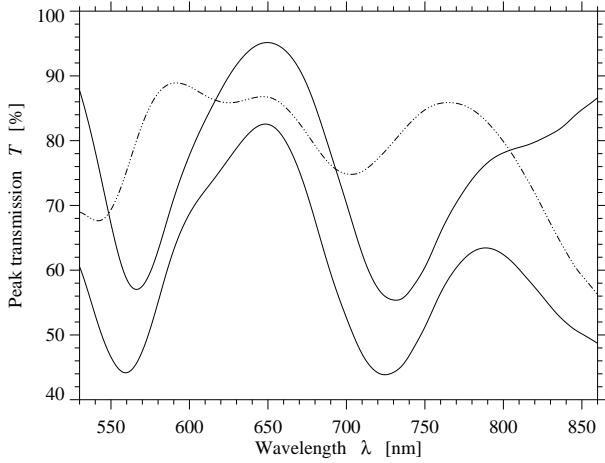


Fig. 8 Peak transmission T_1 of the broad-band (dash-dotted) and T_2 of the narrow-band (thin solid) etalon and the combined peak transmission T (thick solid) of the dual-etalon system.

590–690 nm. The highest transmission of more than 80% is achieved near the strong chromospheric absorption line H α λ 656.28 nm.

310

$$\mathcal{F} = \frac{\text{FSR}}{\text{FWHM}} = \frac{\pi\sqrt{R}}{1-R} \quad (5)$$

The reflectivity finesse \mathcal{F} also enters in the Airy function (Eqs. 1–4) because of its relation to the parameter F .

$$\mathcal{F}^2 = \frac{\pi^2 F}{4} \quad (6)$$

315

However, in real applications, higher order effects have to be considered. Before coating, the etalon surfaces have an optical quality of $\lambda/p = \lambda/200$ as specified by the manufacturer (with p being the plate-defect finesse). After coating p reduces to 140. The nominal finesse \mathcal{F}_{nom} includes the contributions by plate defects.

320

$$\mathcal{F}_{\text{nom}} = \left[\frac{(1-R)^2}{\pi^2 R} + \frac{4}{p^2} \right]^{-1/2} \quad (7)$$

According to Eqs. 1 and 4, the transmission curve of an etalon is a quasi-periodic function. Even in a dual-etalon system, interference filters have to be introduced as order-sorting filters. A dual-cavity interference filter can be constructed using the superposition of two etalons with fixed but almost identical plate spacings, which are slightly displaced from the central wavelength λ_0 . The superposition of two Airy functions (Eqs. 1–4) yields a good approximation of the custom interference filters used at the GFPI, where the details of the manufacturing process are proprietary. The two transmission curves shown in Fig. 9 were constructed to resemble the Fe I λ 543.4 nm and Fe I λ 617.3 nm GFPI filters, which have a FWHM of 0.30 nm and 0.74 nm, respectively. Narrow-band filters of this FWHM provide, as already mentioned in Sect. 2, a good compromise between

325

330

335

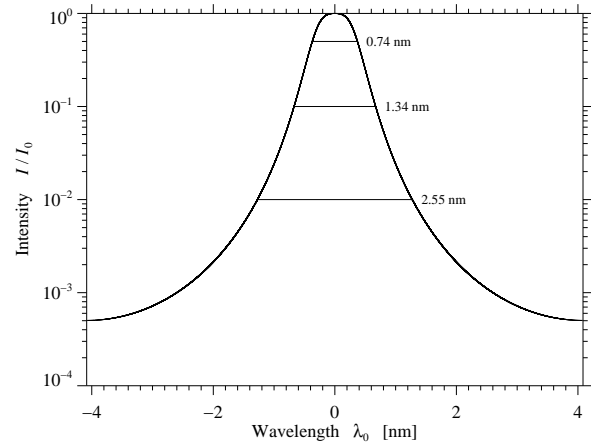
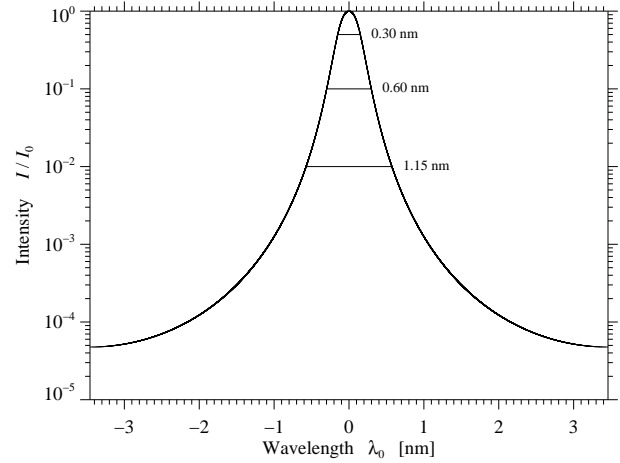


Fig. 9 Transmission profiles of two-cavity interference filters with a FWHM of 0.30 nm (upper panel) and 0.74 nm (lower panel), which are representative for the GFPI pre-filters. The interference filters consist of two superposed Airy functions with a reflectivity $R = 0.87$ and 0.80 and cavity spacing $d = 26 \mu\text{m}$ and $22 \mu\text{m}$, which are displaced by $\pm 0.10 \text{ nm}$ and $\pm 0.26 \text{ nm}$ from the central wavelength λ_0 . Since the combined Airy functions are periodic, they were plotted only between the minima enclosing the maximum at the central wavelength λ_0 . The labels in the plot refer to the width of the interference filters at normalized intensities $I/I_0 = 0.5, 0.1,$ and 0.01 , respectively.

parasitic light, transmission, and signal-to-noise. The overall shape and the width of the interference filters at normalized intensities $I/I_0 = 0.5, 0.1,$ and 0.01 match the specifications provided by the manufacturer (Barr Associates). This type of narrow-band interference filters is commonly used in combination with etalons. This is the reason why we did not use a specific central wavelength λ_0 in Fig. 9.

340

A key parameter to characterize an etalon is the finesse \mathcal{F} , which is basically the free spectral range (FSR) divided by the FWHM of the transmission profile. In the simplest form, the finesse \mathcal{F} can be related to the reflectivity R .

345

Higher order effects such as warping and shrinkage of the coatings are not taken into account in the follow-

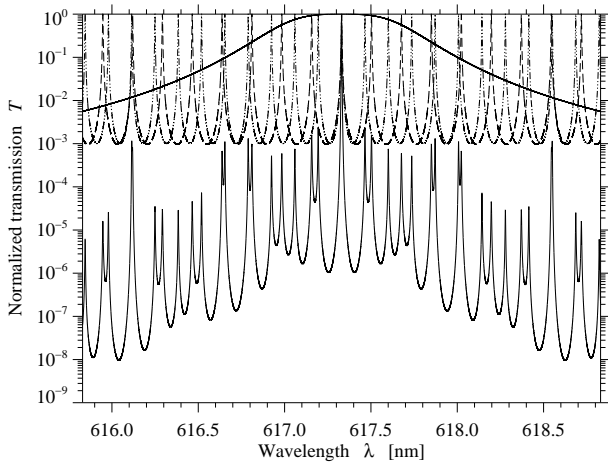


Fig. 10 Transmission profile of the GFPI at Fe I $\lambda 617.33 \pm 1.50$ nm. The curves correspond to a narrow-band interference filter (FWHM = 0.74 nm, thick solid line), etalon 1 ($R = 0.95$, $d = 1.4$ mm, FWHM = 2.1 pm, thin dashed line), etalon 2 ($R = 0.95$, $d = 1.1$ mm, FWHM = 2.7 pm, thin dash-dotted line), and the total transmission curve (FWHM = 1.5 pm). The parasitic-light fraction of the combined filters is about 4.6%.

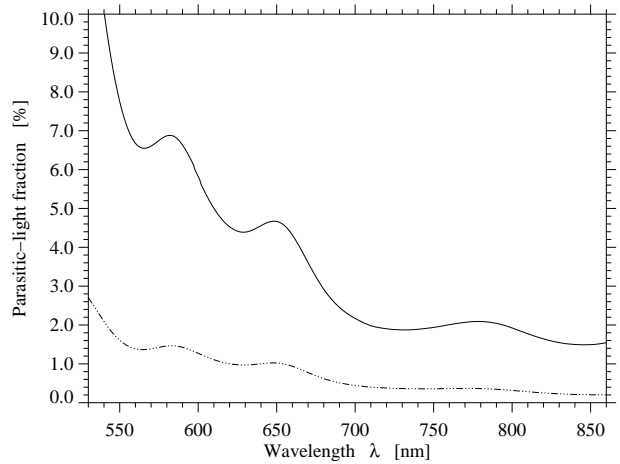


Fig. 11 GFPI parasitic-light fraction for order-sorting interference filters with a FWHM of 0.75 nm (*solid*) and 0.30 nm (*dash-dotted*).

ing calculations, where we assume a constant $p = 140$. The transmission profiles of the individual etalons and the order-sorting interference filter are shown in Fig. 10 for the Fe I $\lambda 617.3$ nm line. The final GFPI transmission profile (thin solid curve) was already multiplied by the transmission curve of the pre-filter (thick solid curve). Out-off band transmission exceeds $I/I_0 = 10^{-3}$ only in a few locations. Typically, secondary transmission peaks reach values of I/I_0 in the order of 10^{-3} – 10^{-5} . The parasitic-light fraction is defined as the ratio of the intensity transmitted out-off band to that of the central transmission peak and has been calculated according to the wavelength range of the pre-filters shown in Fig. 9, i.e., ± 3 nm and ± 4 nm, respectively. In the case presented in Fig. 10, it amounts to about 4.6% because of the relatively wide Fe I $\lambda 617.3$ nm pre-filter (FWHM = 0.75 nm) with high transmission above 80%.

The parasitic-light fraction can be minimized during the design of a dual- or multi-etalon system. However, when the preparations of the GFPI for the GREGOR telescope started in 2005, the first narrow-band etalon with a plate spacing of $d = 1.1$ mm was purchased in addition to an already existing broad-band etalon with $d = 0.125$ mm. The second narrow-band etalon with $d = 1.4$ mm was then purchased later on as the best choice in combination with the etalon with $d = 1.1$ mm, although in principal these plate spacings are not optimal. In Fig. 11, we present the wavelength-dependent parasitic-light fraction for the two interference filters in Fig. 9 and for the characteristic parameters of the dual-etalon system. The two curves represent upper and lower bounds for all narrow-band GFPI interference filters. The way appearance of the curves has its origin in the coat-

ing curves (reflectivity $R_{1,2}(\lambda)$ and absorption $A_{1,2}(\lambda)$) of the etalons. In the case of the 0.75 nm filter, one has to consider the trade-off between high-transmission on the one side and high off-band contributions to the spectral line profile. Below 610 nm the parasitic-light fraction exceeds 5%, which might no longer be acceptable for spectral inversions. Nevertheless, interference filters with a FWHM of 0.3 nm are well-suited to bring the parasitic-light fraction down to much lower values, (e.g., Fig. 11 and Puschmann et al. (2012b), their Fig. 9, left panel). Nowadays, it is also possible to achieve a transmission above 60% for the narrower pre-filters but at additional cost. The choice of a suitable pre-filter is ultimately driven by the science case of GFPI observations.

The spectral resolving power \mathcal{R} of an FPI can be expressed as

$$\mathcal{R} = \frac{\lambda}{\Delta\lambda} = 0.97m\mathcal{F}, \quad (8)$$

where m is the order of interference (Born & Wolf 1998). If the angle of incidence θ is almost normal to the etalon plates, the spectral resolution becomes

$$\mathcal{R} = \frac{\lambda}{\Delta\lambda} \approx \frac{2\mathcal{F}nd}{\lambda} \quad \text{with} \quad \cos\theta \approx 1. \quad (9)$$

Using Eq. 5, we can relate the FSR to the bandpass $\Delta\lambda$ and Finesse \mathcal{F} by

$$\text{FSR} = \frac{\lambda^2}{2nd} = \Delta\lambda\mathcal{F}. \quad (10)$$

This approach can be used for individual etalons. However, to compute the wavelength-dependent spectral resolution $\mathcal{R}(\lambda)$, we first multiplied the individual transmission curves, before computing the FWHM and the equivalent width, i.e., the width of a box-type filter, which transmits the same number of photons. Both curves are presented in Fig. 12. The extended wings of the Airy function result in a larger equivalent width than the FWHM and thus to a lower spectral resolution \mathcal{R} . In both cases, however, we assume

no higher-order effects, which can affect the finesse \mathcal{F} . The highest spectral resolution can be achieved at shorter wavelengths. Again, the shape of the curves has its origin in the coating curves of the etalons. If the finesse changes across the pupil, then the spectral resolution can significantly decrease for almost fully illuminated etalon plates.

During science verification, the dispersion and spectral resolution of the GFPI was determined (Puschmann et al. 2012b, their Tab. 3). In agreement with earlier measurements, the dispersion follows a linear relation

$$\delta\lambda_{\min} = C_0 + C_1\lambda, \quad (11)$$

with the wavelength given in meters and the coefficients $C_0 = 0.93 \times 10^{-14}$ m and $C_1 = 4.63 \times 10^{-7}$. The minimum step width at 530 and 860 nm corresponds thus to 0.25 and 0.40 pm and yields a maximum scan range of 1.02 and 1.63 nm at these edge wavelengths, respectively, given the 12-bit resolution of the CS100 ICOS etalon controllers. With respect to the spectral resolution, we found a significant deviation between the theoretical ($\mathcal{R} = 250,000$) and effective spectral resolution ($\mathcal{R} = 100,000$) using the method described by Allende Prieto et al. (2004) and Cabrera Solana et al. (2007) that estimates the latter by a comparison to a reference profile. At the VTT, Puschmann & Beck (2011) still obtained a spectral resolution of $\mathcal{R} \approx 160,000$ using the same method. However, the pupil image was smaller at the VTT (≈ 40 mm) than at the GREGOR telescope (~ 60 mm). A degradation of the finesse between the central and peripheral etalon regions of about 1.3 was found already for a single etalon for radii of 15 mm and 50 mm by Denker & Tritschler (2005).

One of the advantages of a FPI in a collimated mounting is that each point in the image plane has the same spectral resolution everywhere (Cavallini 2006), which is also higher as compared to similar FPIs in telecentric mounting. In other words, each point in the images essentially receives light from the entire pupil, i.e., any local defect of the plates will diminish the finesse, thus leading to a lower spectral resolution. One approach to mitigate this problem is to widen the beam diameter of the laser (currently 15 mm), which is used to maintain the parallelism of the plates. Sampling a larger area of the etalon plates would result in a better compromise between the contributions by the inner and peripheral parts of the etalon plates to the overall finesse. The application of the above mentioned method to spectra from other spectrometers based on air-spaced etalons would be extremely interesting for comparison.

Reducing the diameter of the pupil image is not a solution to circumvent the above problem, because this would increase the blueshift $\delta\lambda_\theta$ contained in the filtergrams, where the wavelength information of each pixel is field-dependent (see Cavallini 2006) according to

$$\delta\lambda_\theta = -\frac{\lambda\theta^2}{2n}, \quad (12)$$

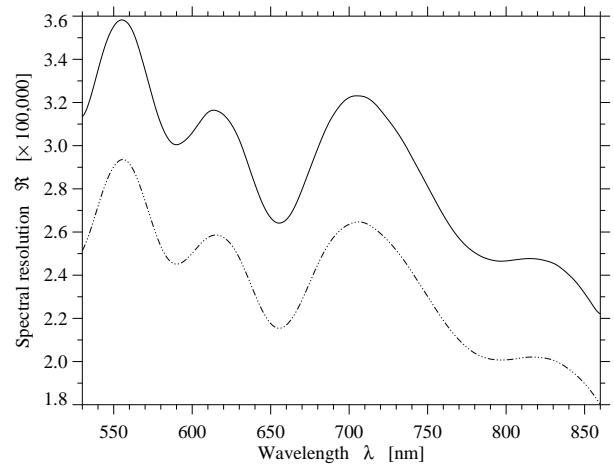


Fig. 12 Spectral resolution \mathcal{R} as a function of wavelength λ based on the FWHM (*solid*) and equivalent width (*dash-dotted*) of the dual-etalon system.

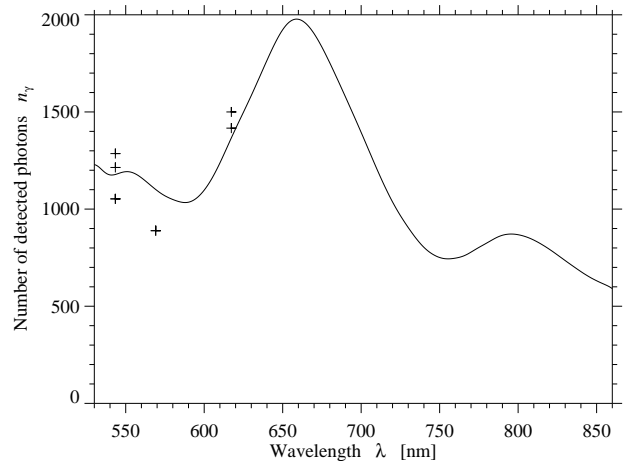


Fig. 13 Number of detected photons n_γ as a function of wavelength λ for an exposure time of $\Delta t = 10$ ms considering the transmission profile of the dual-etalon system, the quantum efficiency of the Sensicam QE camera, and all relevant characteristic parameters of the GFPI (without the transmission of the order-sorting pre-filter). The plus signs refer to actual measurements of the continuum intensity.

where θ is the angle of incidence and n the index of refraction. If the angle of incidence remains small, the Helmholtz-Lagrange invariant yields

$$\beta = \frac{D_{\text{FPI}}}{f_{\#} D_{\text{tel}}}, \quad (13)$$

with the field angle β , the f -number $f_{\#}$ of the optical system, and the diameters of etalons D_{FPI} and telescope aperture D_{tel} . Combining these equations provides the expression

$$\delta\lambda_\theta = -\frac{\lambda}{8n} \left(\frac{\beta D_{\text{tel}}}{D_{\text{FPI}}} \right)^2, \quad (14)$$

which can be used to calculate the blueshift $\delta\lambda_\theta = 3.7\text{--}6.1$ pm for the wavelength range 530–860 nm and a field

angle $\beta = 60''$. Theoretical values and actual measurements of the maximal blueshift across the FOV at wavelengths between 543.4 nm and 630.2 nm are in very good agreement (see Puschmann et al. 2012b, their Tab. 4).

In planning an observing sequence, the number of detected photons n_γ should be known as a function of wavelength λ . Extracting the bandpass from the curves shown in Fig. 12, we can adjust this curve to match GFPI observations as demonstrated in Fig. 13. The overall efficiency of the telescope and other optical components was assumed to be constant at about 4.8% to reach a good agreement between observations and theory. Note that the observations might be affected by the sky transparency, the zenith distance of the Sun, and to a lesser extent by the scene observed on the solar surface. We have excluded the order-sorting interference filter from this comparison, which would further reduce the number of detected photons n_γ , because its characteristics strongly varies with the spectral line chosen for the observations. Typically, a level of $n_\gamma \approx 6000$ photons should be measured in the continuum of a spectral line, i.e., the exposure time Δt and/or the binning have to be adjusted accordingly. In the last computation we took into account a factor of two for the conversion of detected photons in measured electrons in the analog-digital conversion. Thus, the continuum intensity of the quiet Sun would reach about three quarters of the full-well capacity of the Sensicam QE detector. Measured values obtained by Puschmann et al. (2012b) are in good agreement (see the corresponding plus signs in Fig. 13).

5 Polarimetry

A polarimeter can be inserted just in front of the detector in the NBC for using the GFPI in the dual-beam vector spectropolarimetric mode. Both orthogonal beams are imaged on the same chip, thus reducing the available FOV to $25'' \times 38''$. The polarimeter by courtesy of the IAC is described in detail in Bello González & Kneer (2008). It consists of two ferro-electric liquid crystals (FLC) and two polarizing beamsplitters, i.e., calcites. The latter split the light into ordinary and extraordinary beam, which are separated by 4.2 mm. A half-wave plate between the two calcites exchanges both beams. The first FLC acts roughly as a half-wave plate and the second as a quarter-wave plate. FLCs are switched between two states, which allows one to retrieve the full Stokes vector from four independent measurements. An image of the polarimeter is shown in Fig. 14. The FLCs in the silver-colored mounts are located inside the main brass-colored housing and can be rotated against each other. The various cables connect to the power supply and conduct the switch signals to the FLCs. The calcites are mounted near the black-painted exit of the polarimeter to the right. The central black ring connects the polarimeter to the mechanical holder on the optical table.

The projected lengths of the extraordinary beam in the xy - and xz -planes are different when passing the first calcite,



Fig. 14 Image of the Stokes vector polarimeter.

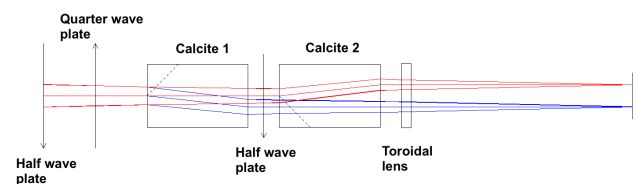


Fig. 15 ZEMAX ray-tracing including polarimeter and a toroidal lens with a curvature radius of 710 mm as corrector for the astigmatism introduced by the polarimeter. From left to right: dual-beam polarimeter with FLC1 ($\lambda/2$), FLC2 ($\lambda/4$), calcite 1, half-wave plate, calcite 2, and at its exit the toroidal lens. Red and blue rays show ordinary and extraordinary beams, respectively.

which introduces astigmatism. The ordinary beam of the first calcite is then affected by the second calcite, producing once more the same amount of astigmatism with the same orientation. The astigmatism can be mostly compensated by a toroidal lens with a curvature radius of 710 mm (see Figs. 15 and 16). The astigmatism caused by double refraction is the dominating aberration followed by spherical aberration and exceeds the Airy disk, which can be easily seen in the spot diagrams for the peripheral wavelengths (left panel of Fig. 16). The compensation for astigmatism and spherical aberration with a weak cylindrical lens (one-dimensional toroid) faced with the curvature towards the calcites compensates both aberrations and gives a diffraction-limited imaging for the central wavelength and just diffraction-limited imaging for the peripheral wavelengths (right panel of Fig. 16). The strength of the aberrations is nearly independent of the field position.

The retardance $\delta_{1,2}$ and cone angle $\alpha_{1,2}$ of the FLCs, and the polarimetric efficiency have been measured in the laboratory at three different wavelengths, i.e., 557 nm, 620 nm, and 656 nm (Table 4). An optimum polarimetric efficiency resulted when the two FLCs were rotated by 20° relative to each other. The efficiencies of about 50% are

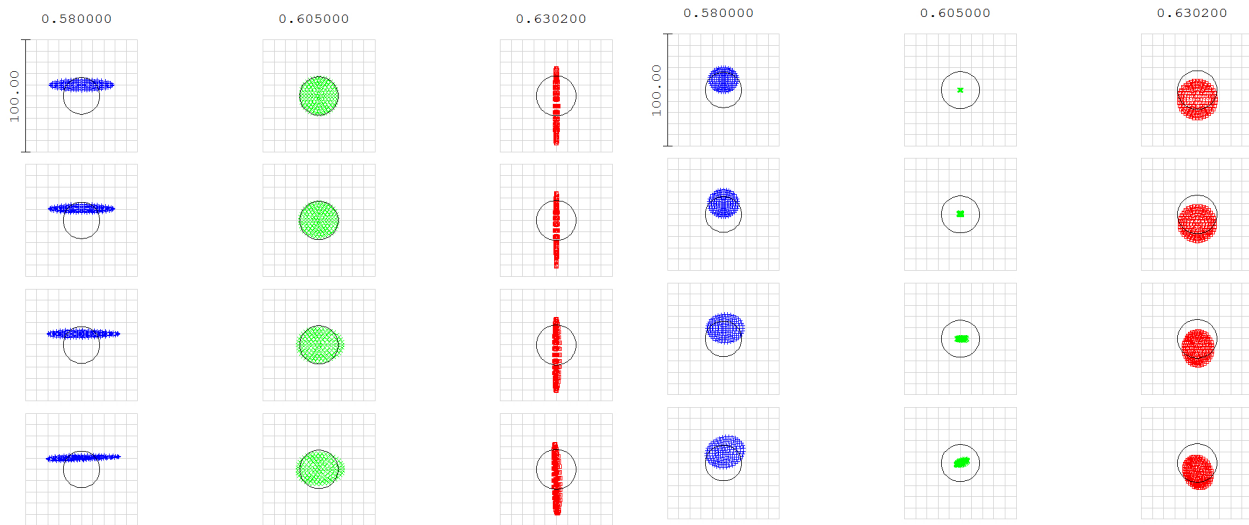


Fig. 16 Matrix spot diagrams (wavelength range 580–630 nm with a focus on 605 nm) for the NBC including the Stokes vector polarimeter. Left panel: without corrector. Right panel: the same including a toroidal lens with a curvature radius of 710 mm as depicted in Fig. 15 as corrector. From top to bottom: central optical axis, and at field positions of $x = 0$ mm, $y = 3$ mm; $x = 5.3$ mm, $y = 0$ mm; $x = 5.3$ mm, $y = 3$ mm.

Table 4 Retardance $\delta_{1,2}$ and cone angle $\alpha_{1,2}$ for FLC 1 and FLC 2, and polarimetric efficiencies ϵ .

FLC 1	δ_1	δ_2	α_1	α_2	$\Delta\alpha$
557 nm	144.0	139.5	51.3	11.8	39.5
620 nm	162.8	155.1	50.1	9.9	40.2
656 nm	163.3	160.8	50.5	10.0	40.5

FLC 2	δ_1	δ_2	α_1	α_2	$\Delta\alpha$
557 nm	100.7	96.5	85.3	41.5	43.8
620 nm	83.0	80.4	86.5	40.5	46.0
656 nm	78.4	80.4	58.4	17.6	40.8

ϵ	$\epsilon(I)$	$\epsilon(Q)$	$\epsilon(U)$	$\epsilon(V)$	ϵ_{total}
557 nm	0.978	0.565	0.519	0.518	0.926
620 nm	0.971	0.585	0.481	0.620	0.979
656 nm	0.430	0.191	0.200	0.366	0.459

telescope was developed (Balthasar et al. 2011; Hofmann et al. 2012). Together with regular calibration measurements during the observing campaigns using the GPU, this model will serve to calibrate the spectropolarimetric data taken with both the GFPI and GRIS.

However, the GPU can currently only be used for polarimetric calibrations in the near-infrared wavelength range because of thermal issues with the retarders at visible wavelengths. An additional protection with a partly transparent mirror in front of the GPU is planned to reduce the heat load. A second calibration unit (Collados et al. 2012) is foreseen for both the visible and near-infrared spectral range. This unit will be inserted behind the telescope exit in the observing room to determine the instrumental polarization of the static optical path of AO system and the post-focus instruments. Until the full availability of one or both calibration units in the next year, the observations with the GFPI are restricted to the spectroscopic mode. The implementation of an automated calibration procedure for the GFPI is expected to be finished along with the upgrade of the calibration unit(s). An extension of the usable wavelength range of the polarimeter to 530–860 nm by the addition of one variable FLC retarder (see Tomczyk et al. 2010) is under investigation. However, it is a major task to eventually enlarge the usable FOV in the spectropolarimetric mode. The replacement of the Sensicam cameras by modern, large-format sCMOS cameras as described in Puschmann et al. (2012b) would lead to both higher frame rates and a larger FOV. However, the larger FOV also requires a re-design or replacement of the polarimeter itself, because at present the FOV is also limited by the size of the calcites.

quite good for 557 nm and 630 nm, but they are not satisfactory at 656 nm with about 20% efficiency only.

For accurate polarimetric measurements, a calibration of the complete optical train up to the polarimeter must be performed (Beck et al. 2005a,b; Collados 2003). For this purpose, the GREGOR Polarimetric calibration Unit (GPU, Hofmann et al. 2009, 2012) can be inserted close to the secondary focus F2 of the telescope. The GPU polarizes the incident light in a defined and known way. However, the internal rotations of the alt-azimuthally mounted telescope change the instrumental polarization quite rapidly, therefore a time-dependent polarization model of the GREGOR solar

6 Science with imaging spectropolarimeters

Imaging spectropolarimeters have been used in solar physics for more than two decades and produced a wealth of scientific results. Looking more closely at previous scientific studies with imaging spectropolarimeters – such as the Göttingen Fabry-Pérot Interferometer (Bendlin et al. 1992) and the Telecentric Etalon Solar Spectrometer (TESOS, Tritschler et al. 2004a) at the VTT, the CRISP instrument (Scharmer et al. 2008) at the 1-meter Swedish Solar Telescope, the Interferometric BIdimensional Spectrometer (IBIS, Cavallini 2006; Reardon & Cavallini 2008) at the Dunn Solar Telescope, and the Imaging Magnetograph eXperiment (IMaX, Martínez Pillet et al. 2011) for the Sunrise Balloon-Borne Solar Observatory – reveals the strengths of these instruments to easily adapt to science cases ranging from the quiet Sun to the dynamics of sunspots while covering photospheric as well as chromospheric lines.

The polarimetric accuracy of imaging spectropolarimeters is a few 10^{-3} in terms of the continuum intensity, which is sufficient to follow the coalescence, fragmentation, and cancellation of small-scale magnetic features. Vitičić et al. (2009) studied their association with G-band bright points and used the SIR (Stokes inversions based on response function) approach (Ruiz Cobo & del Toro Iniesta 1992) to determine that their temporal evolution is related to the filling factor rather than to the magnetic field strength. Observations with high polarimetric sensitivity revealed that magnetic fields occupy approximately 45% of the area in internetwork patches, predominantly in intergranular spaces (Domínguez Cerdeña et al. 2003). Scrutinizing the intricate fine structure of granules, Steiner et al. (2010) found evidence for horizontally oriented vortex tubes, i.e., striations with leading bright rim and a trailing dark edge, which migrate in unison from the periphery to the granule's interior.

The infrared Ca II $\lambda 854.2$ nm line is an excellent diagnostics tool (Cauzzi et al. 2008), because photospheric conditions can be examined in its far wings, whereas the line core is exclusively of chromospheric origin. High-cadence observations are a prerequisite to measure oscillations in the photosphere, e.g., Vecchio et al. (2007) identified network magnetic elements, which guide low-frequency oscillations from the photosphere into the chromosphere. Type II spicules have also received much attention, because of their role in providing hot material to the chromosphere (Langanen et al. 2008) and thus contribute to the energy balance of the lower solar atmosphere. High-speed jets were observed in the chromospheric H α $\lambda 656.3$ nm (≈ 50 km s $^{-1}$) and infrared Ca II $\lambda 854.2$ nm (≈ 20 km s $^{-1}$) lines by Rouppe van der Voort et al. (2009), who consider them as on-disk counterparts of type II spicule.

Imaging spectropolarimetry of sunspots has been mainly concerned with the fine structure of the penumbra. A comprehensive study of a regular sunspot with a light-bridge and umbral dots was presented by Tritschler et al.

(2004b), who used maps of the line-of-sight velocity, the line width, the equivalent width, and the line depression for a comprehensive description of sunspot dynamics. The elusive process of penumbra formation has been followed in detail in a four-hour time-series presented in Schlichenmaier et al. (2010). The “uncombed” nature of penumbral filaments, their association with the Evershed flow, and their “sea serpent”-like extension beyond the sunspot's boundaries have been examined by Bello González et al. (2005). More recently, Scharmer et al. (2011) detected ubiquitous downflows (up to 1.0 km s $^{-1}$) in the inner penumbra and a strong Evershed flow (3.0–3.5 km s $^{-1}$) in the outer penumbra, pointing one more time to the complex and very dynamic nature of sunspots.

The investigations described above only present a small cross-section of potential science cases for imaging spectropolarimetry. Every time when high-cadence and high-spatial resolution observations are required to unravel the physics of dynamic solar features, the GFPI and its cousins are the instruments of choice.

7 First observations with adaptive optics

Figure 17 shows the results of one of the first two-dimensional spectral scans obtained at the GREGOR telescope with the GFPI and real-time correction by GAOS on 31 July 2012. A 22-min time series of the active region NOAA 11530 located at S24 W18 (heliocentric angle $\theta = 30^\circ$) was observed between 8:04 and 8:26 UT. The angle between solar south and the center of symmetry was 33.8° . Therefore, the direction from center to limb corresponds approximately to the x -axis. We scanned the Fe I $\lambda 617.3$ nm line with 86 steps and a step size of $\Delta\lambda = 1.17$ pm, taking eight narrow-band images (FWHM = 2.1 pm) at each wavelength position. Broad-band images (FWHM = 10 nm) at 620 nm were simultaneously recorded. The exposure time was 20 ms and each line scan took 64 s. We used a 2×2 on-chip binning corresponding to a spatial sampling of $0''.072$, which resulted in a total FOV of ~ 36 Mm \times 27 Mm. The data reduction included, apart from routine tasks such as flatfielding, a speckle reconstruction of the broad-band data (de Boer 1993; Puschmann & Sailer 2006) and a subsequent deconvolution of the narrow-band data with a modified version of the code by Janssen (2003) that is based on the method of Keller & von der Lühe (1992). The narrow-band data were corrected for the blueshift across the FOV after the deconvolution. Subsequently, the image rotation caused by the alt-azimuthal mount of the GREGOR telescope ($\sim 6^\circ$ in 20 min) was compensated and the data were spatially aligned. Line parameters calculated from the spectra are shown in Fig. 17, together with the speckle-reconstructed broad-band image. The final FOV is reduced to 27 Mm \times 16 Mm because of the data reduction described above and an additional apodisation using a sub-sonic filter with a cutoff-velocity of 5 km s $^{-1}$.

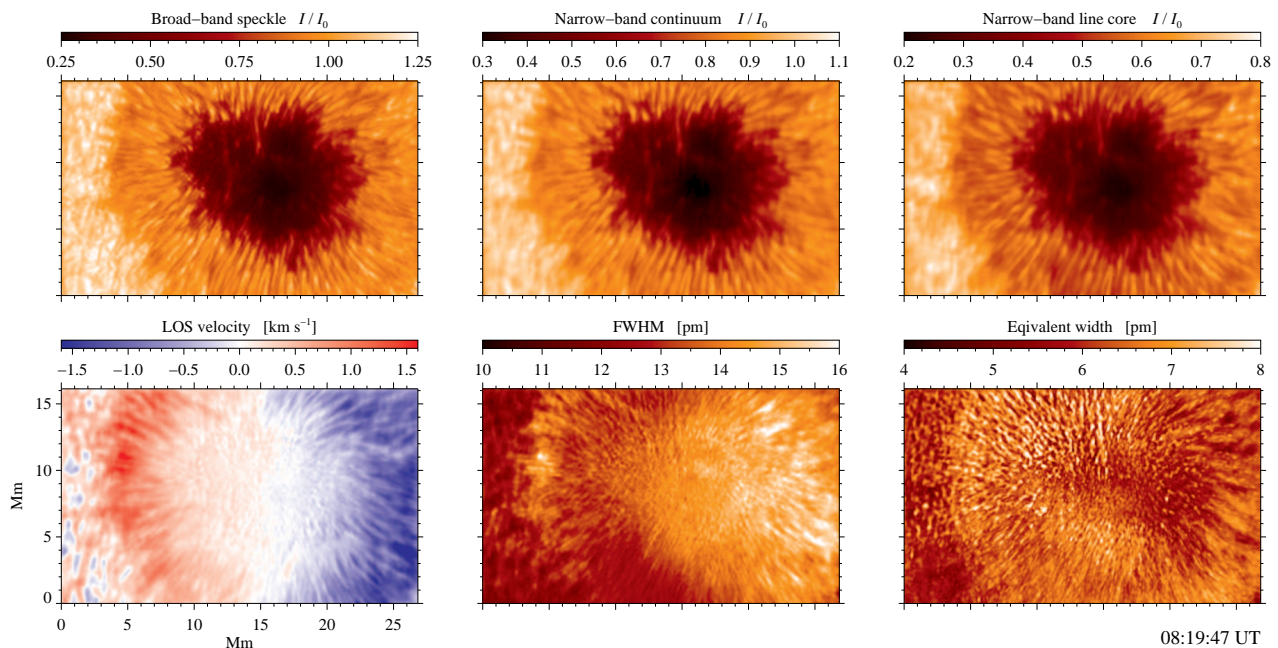


Fig. 17 Example snapshot of a 22-min time series of NOAA AR 11530. Upper panels: speckle-reconstructed broad-band image at 620 nm (left), speckle-deconvolved continuum (middle) and line-core (right) narrow-band images. Bottom panels: line-core velocity (left), full-width at half-maximum (middle), and equivalent width (right).

The contrast of the speckle-deconvolved spectral continuum and line-core narrow-band images is somewhat below that of the speckle-reconstructed broad-band image, but individual umbral dots are still easy to identify. The line-of-sight velocity map clearly reveals the filamentary structure of the penumbra, with strong outflows related to intraspines and velocities close to zero in the spines.

As far as the spatial resolution is concerned, a minimization of the straylight problem currently present at the GREGOR telescope will improve significantly the performance of GAOS in the near future. At the same time, we try to improve the performance of both speckle and blind deconvolution methods by adjusting them to the specific conditions at GREGOR. Thus, we expect that very soon deconvolved spectra near the diffraction limit will be regularly available.

8 Conclusions

The GREGOR Fabry-Pérot Interferometer is designed for imaging spectroscopy (spectropolarimetry) in the range of 530–860 nm (580–660 nm) with a diffraction-limited performance at a spatial sampling of $0''.036$ and a theoretical spectral resolution of $\mathcal{R} = 250,000$. Options for the extension of the wavelength range for polarimetry to 530–860 nm are under investigation. The technical performance of the instrument was verified by direct measurements with the GFPI at the GREGOR telescope during science verification (Puschmann et al. 2012b). Most characteristic parameters of the instrument complied with the theoretical expectations. However, a strong deviation between theoretic

cal and measured spectral resolution was found, which will require some investigation before the next observing campaign. The above mentioned measurements also revealed the need for improving the total throughput for spectropolarimetric observations by either using high-transmission (80%) pre-filters or a 2×2 on-chip binning until new cameras will be available.

The first 2D-spectra obtained with AO support by the end of July 2012 show a very good performance of the GFPI. The instrument is ready, awaiting its users with automatic observing sequences that provide an easy access to scientific observations. An almost completed data reduction pipeline, which also includes image restoration techniques, will further provide an easy handling of the GFPI high-spatial resolution data.

Acknowledgements. The 1.5-meter GREGOR solar telescope was built by a German consortium under the leadership of the Kiepenheuer-Institut für Sonnenphysik in Freiburg with the Leibniz-Institut für Astrophysik Potsdam, the Institut für Astrophysik Göttingen, and the Max-Planck-Institut für Sonnensystemforschung in Katlenburg-Lindau as partners, and with contributions by the Instituto de Astrofísica de Canarias and the Astronomical Institute of the Academy of Sciences of the Czech Republic. CD was supported by grant DE 787/3-1 of the Deutsche Forschungsgemeinschaft (DFG). We would like to thank Robert Geissler for his competent and extended help during the science verification.

References

- Allende Prieto, C., Asplund, M., & Fabiani Bendicho, P.: 2004, *A&A* 423, 1109
- Balthasar, H., Bello González, N., Collados, M., et al.: 2009, in: K.G. Strassmeier, A.G. Kosovichev, J.E. Beckman (eds.), *Cosmic Magnetic Fields: From Planets, to Stars and Galaxies*, IAU Symp. 259, 665
- Balthasar, H., Bello González, N., Collados, M., et al.: 2011, in: J.R. Kuhn et al. (eds.), *Solar Polarization Workshop 6*, ASPC 437, 351
- Beck, C., Schlichenmaier, R., Collados, M., et al.: 2005a, *A&A* 443, 1047
- Beck, C., Schmidt, W., Kentischer, T., & Elmore, D.: 2005b, *A&A* 437, 1159
- Berkefeld, T., Schmidt, D., Soltau, D., et al.: 2012, *AN* 333, 863
- Bendlin, C., Volkmer, R., & Kneer, F.: 1992, *A&A* 257, 817
- Bello González, N. & Kneer, F.: 2008, *A&A* 480, 265
- Bello González, N., Okunev, O.V., Domínguez Cerdeña, I., et al.: 2005, *A&A* 434, 317
- Born, M. & Wolf, E.: 1998, *Principles of Optics*, 6th ed., University Press, Cambridge
- Cabrera Solana, D., Bellot Rubio, L. R., Beck, C., et al.: 2007, *A&A* 475, 1067
- Cauzzi, G., Reardon, K.P., Uitenbroek, H., et al.: 2008, *A&A* 480, 515
- Cavallini, F.: 2006, *SoPh* 236, 415
- Collados, M.: 2003, in: S. Fineschi (ed.), *Polarimetry in Astronomy*, Proc. SPIE 4843, 55
- Collados, M., Calcines, A., Díaz, J.J., et al.: 2008, in: I.S. McLean, M.M. Casali (eds.), *Ground-Based and Airborne Instrumentation for Astronomy II*, Proc. SPIE 7014, 5Z
- Collados, M., López, R., Páez, E., et al.: 2012, *AN* 333, 872
- de Boer, C.R.: 1993, PhD Thesis, Georg-August Universität Göttingen, Germany
- Denker, C. & Tritschler, A.: 2005, *PASP* 117, 1435
- Denker, C.: 2010, *AN* 331, 648
- Denker, C., Balthasar, H., Hofmann, A., et al.: 2010, in: I.S. McLean, S.K. Ramsay, H. Takami (eds.), *Ground-Based and Airborne Instrumentation for Astronomy III*, Proc. SPIE 7735, 6M
- Domínguez Cerdeña, I., Kneer, F., & Sánchez Almeida, J.: 2003, *ApJL* 582, 55
- Halbgewachs, C., Caligari, P., Glogowski, K., et al.: 2012, *AN* 333, 840
- Hofmann, A., Rendtel, J., Arlt, K.: 2009, *Centr. Eur. Astrophys. Bull.* 33, 317
- Hofmann, A., Arlt, K., Balthasar, H., et al.: 2012, *AN* 333, 854
- Kneer, F. & Hirzberger, H.: 2001, *AN* 322, 375
- Janssen, K.: 2003, PhD Thesis, Georg-August Universität Göttingen, Germany
- Keller, C.U. & von der Lühse, O.: 1992, *A&A* 261, 321
- Kneer, F., Al, N., Hirzberger, J., Nicklas, H., & Puschmann, K.G.: 2003, *AN* 324, 302
- Koschinsky, M., Kneer, F., & Hirzberger, J.: 2001, *A&A* 365, 588
- Langangen, Ø., de Pontieu, B., Carlsson, M., et al.: 2008, *ApJL* 679, 167
- Martínez Pillet, V., del Toro Iniesta, J.C., Álvarez-Herrero, A., et al.: 2011, *SoPh* 268, 57
- Puschmann, K.G., Kneer, F., Seelemann, T., & Wittmann, A.D.: 2006, *A&A* 451, 1151
- Puschmann, K.G. & Sailer, M.: 2006, *A&A* 454, 1151
- Puschmann, K.G., Kneer, F., Nicklas, H., & Wittmann, A.D.: 2007, in: F. Kneer, K.G. Puschmann, A.D. Wittmann (eds.), *Modern Solar Facilities – Advanced Solar Science*, p. 45
- Puschmann, K.G., Balthasar, H., Bauer, S.-M., et al.: 2012a, in: T.R. Rimmele (ed.), *Magnetic Fields from the Photosphere to the Corona*, ASPC 463, in press, [ArXiv e-prints, 1111.5509](#)
- Puschmann, K.G., Balthasar, H., Beck, C., et al.: 2012b, in: I.S. McLean, S.K. Ramsay, H. Takami (eds.), *Ground-Based and Airborne Instrumentation for Astronomy IV*, Proc. SPIE 8446, in press, [ArXiv e-prints, 1207.2084](#)
- Puschmann, K.G. & Beck, C.: 2011, *A&A* 533, A21
- Reardon, K.P. & Cavallini, F.: 2008, *A&A* 481, 897
- Roupe van der Voort, L., Leenaarts, J., de Pontieu, B., et al.: 2009, *ApJ* 705, 272
- Ruiz Cobo, B. & del Toro Iniesta, J.C.: 1992, *ApJ* 398, 375
- Scharmer, G.B., Henriques, V.M.J., Kiselman, D., & de la Cruz Rodríguez, J.: 2011, *Science* 333, 316
- Scharmer, G.B., Narayan, G., Hillberg, T., et al.: 2008, *ApJL* 689, 69
- Schlichenmaier, R., Rezaei, R., Bello González, N., & Waldmann, T.A.: 2010, *A&A* 512, L1
- Schmidt, W., von der Lühse, O., Volkmer, R., et al.: 2012a, in: T.R. Rimmele, (ed.) *Magnetic Fields from the Photosphere to the Corona*, ASPC 463, in press, [ArXiv e-prints, 1202.4289](#)
- Schmidt, W., von der Lühse, O., Volkmer, R., et al.: 2012b, *AN* 333, 796
- Steiner, O., Franz, M., Bello González, N., et al.: 2010, *ApJL* 723, 180
- Tomczyk, S., Casini, R., de Wijn, A.G., et al.: 2010, *Ap.Opt.* 49, 3580
- Tritschler, A., Bellot Rubio, L.R., & Kentischer, T.J.: 2004a, *AAS* 204, 6902
- Tritschler, A., Schlichenmaier, R., Bellot Rubio, L.R., et al.: 2004b, *A&A* 415, 717
- Vecchio, A., Cauzzi, G., Reardon, K.P., et al.: 2007, *A&A* 461, 1
- Viticchié, B., del Moro, D., Berrilli, F., et al.: 2009, *ApJL* 700, 145
- Volkmer, R., Kneer, F., & Bendlin, C.: 1995, *A&A* 304, L1
- Volkmer, R., von der Lühse, O., Denker, C., et al.: 2010, *AN* 331, 624
- von der Lühse, O., Volkmer, R., Kentischer, T., et al.: 2012, *AN* 333, 894